www.czasopisma.pan.pl PAN www.journals.pan.pl

Metrol. Meas. Syst., Vol. 24 (2017), No. 4, pp. 617–630.

PAN POLSKA AKADEMIA NAUK

METROLOGY AND MEASUREMENT SYSTEMS

Index 330930, ISSN 0860-8229

www.metrology.pg.gda.pl

M&MS

ANALYSIS OF PROPERTIES OF AN ACTIVE LINEAR GESTURE SENSOR

Krzysztof Czuszyński, Jacek Rumiński, Jerzy Wtorek

Gdańsk University of Technology, Faculty of Electronics Telecommunications and Informatics, G. Narutowicza 11/12, 80-233 Gdańsk, Poland (✉ krzysztof.czuszynski@pg.edu.pl, +48 58 347 1725, jacek.ruminski@pg.edu.pl, jerzy.wtorek@pg.edu.pl)

Abstract

Basic gesture sensors can play a significant role as input units in mobile smart devices. However, they have to handle a wide variety of gestures while preserving the advantages of basic sensors. In this paper a user-determined approach to the design of a sparse optical gesture sensor is proposed. The statistical research on a study group of individuals includes the measurement of user-related parameters like the speed of a performed swipe (dynamic gesture) and the morphology of fingers. The obtained results, as well as other *a priori* requirements for an optical gesture sensor were further used in the design process. Several properties were examined using simulations or experimental verification. It was shown that the designed optical gesture sensor provides accurate localization of fingers, and recognizes a set of static and dynamic hand gestures using a relatively low level of power consumption.

Keywords: optical sensor, gestures, mobile devices, Monte Carlo Simulation, smart glasses.

1. Introduction

The development of mobile devices and a wide range of their possible applications have stimulated extensive research on possible interaction methods, especially those related to the design of low-power gesture sensors. Touchless interfaces are of special interest as they could prove useful in some specific areas, *e.g.* in healthcare [1, 2]. Let us focus on basic optical sensors; to date they have been mainly used as supplementary input devices in mobile equipment like smartphones and tablets. Three types of power-effective basic optical gesture sensors can be distinguished regarding the number of light-sensitive elements (detectors) of the device.

The first type are one-detector sensors. They can detect a proximity level [3], a swipe event along a single axis and a dynamic pose of hand [4, 5]. To determine the swipe direction while only having one LED, the sensitivity gradient [5], light inhibitor [6] or asymmetric optical blocks [7] can be applied. Solutions involving two light sources are also used [8]. The second type are two-detector sensors. One- and two-detector sensors, which mainly recognize swipe events are called *Motion Gesture Sensors* (MGSs) [9, 10]. They can estimate the direction and often the speed of detected movement, but not a precise range of swipe. The third type are sensors with several detectors, excluding matrices of detectors, like RGB cameras. Kong *et al.* have proposed three-detector MGSs with [11] and without [12] optical blocks enclosed in a single chip, handling swipes in 3D. Withana *et al.* have proposed a modular sensor composed of photodiode-LED pairs [13], which can be arranged in a linear or triangular form. It can handle a wide variety of gestures but it is not able to localize a hand precisely. They have also described a two-emitter, six-receiver prototype sensor for virtual reality glasses, which detects swipes and push/pull gestures [14]. Chuang *et al.* have mounted emitter-receiver pairs in the corners of a mobile device that enabled to recognize a hand position basing on trilateration [15]. Tang *et al.* have proposed a linear, 10-detector IR transceiver, as an implementation of the

Article history: received on Feb. 08, 2017; accepted on May 21, 2017; available online on Dec. 01, 2017; DOI: 10.1515/mms-2017-0052.

virtual computer mouse, which tracks a hand position and can detect three click gestures [16]. A similar solution was applied to multi-touch interactions with a mobile device, mounted at the edges of its housing [17]. The gestures based on tracking eyeball movements, recorded by 4 photodiode-LED pairs per eye, were examined as well [18].

Considering the gestures' taxonomy, MGSs mostly detect motion-related events (dynamic gestures) but also the presence of a still hand (static gesture). In *human system interactions* (HSI), both of these gesture types are discrete. This means that the system responds after a whole gesture is completed (or its duration exceeds a threshold). Some interfaces handle continuous gestures, *e.g.* [15]. In terms of HSI, the system navigated by such an interface reacts while the gesture is performed.

As indicated, basic optical gesture sensors often handle a narrow set of gestures, mainly using a discrete dynamic. But when more gestures can be directly associated with varied actions the system response becomes more rapid and more precise. Moreover, there are not many basic optical sensors, which can handle both continuous and wide sets of discrete gestures. Therefore, the intension of this work is to design a touchless, power-efficient, several-detector optical sensor, capable of handling a wide set of both discrete and continuous gestures. The aim of the paper is to adjust the parameters of the proposed construction of a sensor, so that it would be capable of detecting certain hand movements and differentiating various hand arrangements, while respecting user-defined spatiotemporal requirements. The study is based on simulations and experiments carried out with the use of actual implementation of the sensor.

The paper is organized as follows: the first section contains the introduction, an outline of the state-of-the-art technology and the objective of the work. The second section presents the methods applied to describe and measure the performance of the proposed optical sensor. The obtained results of simulations and experiments are included in the third section. The summary and conclusions are given in the last section.

2. Materials and methods

2.1. Proposed sparse optical gesture sensor

Basing on initial requirements and the present state-of-the-art, a prototype of the sparse construction of optical gesture sensor with 8 aligned IR *photodiodes* (PD) has been designed (Fig. 1a). The photodiodes are evenly distributed on an 8 cm long *printed circuit board* (PCB), with 4 IR LEDs. All optical elements are mounted on the same plane and face in one direction. The applied photodiodes are chips with built-in operational amplifiers TSL260RD and the used LEDs are KA-3528SF4S. The sensor's microprocessor, a 5 V supplied PIC24FV16KA302, is employed in data sampling, processing and duplex communication via a UART serial interface.

The distributions of PDs and LEDs on the PCB are denoted by d_{PD} and d_{LED}, respectively. In the design the LEDs are placed along an axis designated by photodiodes and each is separated from the closest PD by $d_{PD}/2$. A sensor is considered sparse when $d_{PD} \geq 5a$, where a is the side of the active area of a square-shaped PD. The angular parameters of optoelectronic elements are described by β_{PD} and β_{LED} – the field of view of elements (FOV) – which can be adjusted by the application of optical blocks of appropriate height (h_{bPD}, h_{bLED}). They can be modified together using a set of overlays created with the 3D printing technology. The angular sensitivity of PDs and LEDs is assumed to be a cosine function. The position of each element within the sensor is described in the Cartesian coordinate system, with the origin located between two middle PDs, (Fig. 1b). The position of the centre of active area of an optoelectronic element is defined by the coordinates of that element.

Metrol. Meas. Syst., Vol. 24 (2017), No. 4, pp. 617–630.

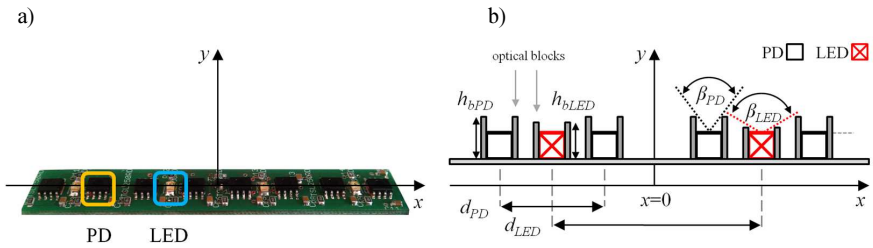

Fig. 1. An optical gesture sensor (without optical blocks for better clarity) (a). A sketch of the sensor descriptive parameters – a side view of the central part of the sensor (b).

A sparse optical gesture sensor analyses the pattern of light intensity obtained from the PDs. It can operate in two modes, depending on the *ambient light* (AL) level. In strong AL conditions, the pattern of shadow caused by a hand covering the light is analysed. In weak AL conditions, the pulses of sensor LEDs highlight a hand performing a gesture and the pattern of reflected light is analysed. These modes are called the passive and active ones, respectively. In this paper only the active operating mode is considered. The pattern is to be produced by the shadow created by the hand performing a gesture; it indicates the arrangement of fingers. Two types of pose are considered. *Spread* (S) indicates that all of the *fingers* (F) involved in the gesture are separated, in opposition to the *Joined* (J) fingers' arrangement. The codes of gestures are presented in Table 1.

Table 1. The codes of static discrete gestures to be handled by the sparse optical sensor.

Fingers involved	**1**	**2**	**3**	**4**
Spread arrangement	1FS	2FS	3FS	4FS
Joined arrangement	–	2FJ	–	4FJ

2.2. User studies

The research on a control group of individuals was performed in order to gain referential requirements for the sensor design in terms of physical dimensions and throughput of the system. The group consisted of 41 Caucasian volunteers (21 females, 20 males, age: 26.4 ± 6.1 years).

In the first part of the experiment the following parameters were measured: R, a radius of an index finger (1FS), $D2$, a width of an index and middle fingers joined (2FJ) and L, a spacing between the centres of middle and index fingers while freely arranged (2FS).

In the next part, the volunteers were asked to perform three series of swipe gestures along the sensor, at a distance of about 1−5 cm. Each series: 2FJ slow swipe, 2FJ fast swipe and 2FS fast swipe consisted of 5 repetitions. The gestures were recorded with a referential sampling frequency, $f_r = 2$ kHz, in order to precisely measure the velocity of the movements. The signals were sampled directly from the output of photodiode chips using a USB-1608GX DAQ device. The optical sensor was set to full light mode ($D = 100\%$).

2.3. Sensor design features

The sensor's abilities of recognition and handling of different gestures result from its properties. They have been described by a set of parameters, which are discussed and evaluated in the following subsections.

2.3.1. Illumination pattern flatness

Let the numbers of photodiodes and LEDs, n_{PD}, n_{LED} respectively, and both d_{PD}, d_{LED}, define a specific formation of optical elements within a sparse gesture sensor. Three different formations were initially examined in this paper (Fig. 2).

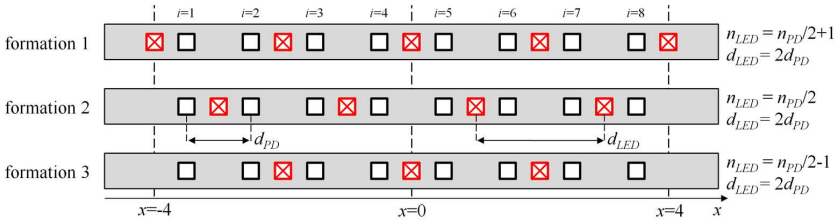

Fig. 2. Three types of formations of optoelectronic elements (top view) within a sparse linear sensor. Optical blocks are not presented for the sake of clarity of the figure.

Each of them creates its own illumination pattern differing in flatness along x and y axes. The greater the $flatness_y$ (on the y axis), the greater the effective range of the sensor (photodiodes saturate further from the device). A greater $flatness_x$ (along x axis) enables a more linear estimation of the hand position when no correction is applied. Consider a flat, w cm wide, obstacle positioned centrally above the most inner and most outer photodiodes at a distance h from the sensor in two separate measurements. The $flatness_x$ is calculated as a ratio of the strengths of signals from the most outer (second measurement) and most inner (first measurement) photodiodes (in the case of n_{PD} = 8, 1st/8th and 4th/5th respectively). The $flatness_y$ is expressed as a $flatness_x(h)$ function.

2.3.2. Operating area

Kim *et al.* have described their two-detector sensor with three zones [9]. An obstacle (hand/fingers performing a gesture) is in the dead zone when any of the detectors can see it. In a linear sensor, considering a 2D section, there are n_{PD} + 1 triangular dead zones (Fig. 3). However, in the active operating mode, the obstacle has to be within the FOV of both detectors and light sources. Therefore, the illumination system has its own dead zone as well. The heights of the dead zones of detectors and the illumination system can be respectively described by:

$$h_{ddz} = d_{PD} / \left(2tg(\beta_{PD} / 2)\right), \qquad h_{idz} = d_{LED} / \left(2tg(\beta_{LED} / 2)\right). \tag{1}$$

When an object is located closer than at the operating distance h_{op} = min(h_{ddz},h_{idz}), its visibility depends on its location along the x axis. In this area indistinct results are obtained, hence it is called an ambiguous zone and it has to be minimized. The obstacle delivers proper data for gesture recognition if located in the detectable zone, at $h \geq h_{op}$. A width of the detectable zone, l (Fig. 3), at height h, for a sparse linear sensor composed of n_{PD} photodiodes can be described as:

$$l(h) = (n_{PD} - 1)d_{PD} + 2h \cdot tg(\beta_{PD} / 2). \tag{2}$$

The sensor is dedicated to detection of close range gestures. Hence, the upper range limit is assumed to be h_{max} = 5 cm, since interference with objects located further away is undesirable. As the sensor is touchless, the minimum operating distance considered, where contact with the device could be avoided, is h_{min} = 1 cm, hence $h_{op} \leq h_{min}$.

Metrol. Meas. Syst., Vol. 24 (2017), No. 4, pp. 617–630.

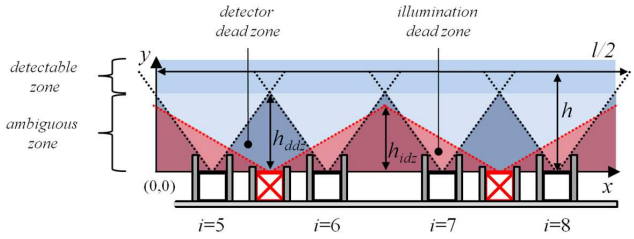

Fig. 3. A sketch of the right side of the sparse optical sensor with three types of zones marked.

2.3.3. Resolving power

An important property of the sensor is its ability to differentiate FS and FJ arrangements (*e.g.* 2FS vs 2FJ). Therefore, a distance at which the sensor detects an indentation in the pattern of reflected light intensity produced by a gap in 2FS, should be maximized. In the 2FS, fingers of radius R are separated from each other by L (Fig. 4a). The depth of indentation, I_D, in an observable pattern (Fig. 4b) is the separation criterion. Lack of indentation means that L of fingers in 2FS at h is too small for a given set of parameters of the sensor. Therefore, the impact of d_{PD} and β_{PD} on the resolving power of the sensor along two axes is considered. The *shift* parameter is a distance between the centre of symmetry of a sensor ($x = 0$) and the x component of the centre of symmetry of a given fingers' arrangement system (Fig. 4a). The variability of I_D as a function of *shift*, h for fixed R and L values is of interest. The I_D is obtained from:

$$I_D = 1 - \frac{v_M}{\min(v_L, v_R)}, \tag{3}$$

where v_L and v_R are values of peaks adjacent to the common middle value v_M from the left and right sides, respectively (Fig 4b).

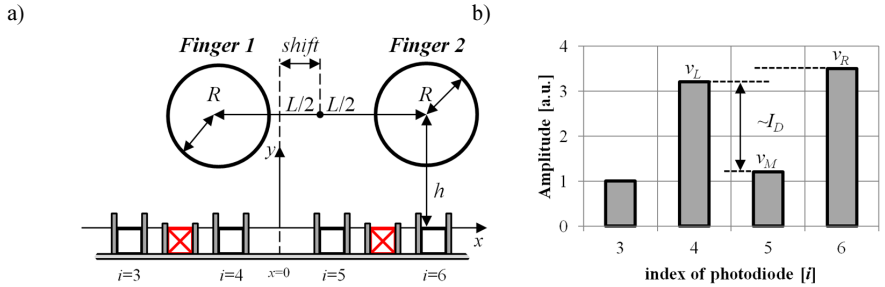

Fig. 4. A cross-section of the middle part of the sensor and fingers in the 2FS arrangement (a). A corresponding light intensity pattern with the meaningful values for calculation of indentation depth, I_D (b).

2.3.4. Spatial and temporal sensitivity

Motion detection describes the minimal distance covered by a hand which causes a detectable swipe at a distance h [11]. In the sparse sensor, the spatial sensitivity can be defined as the minimal noticeable displacement of an obstacle moving along the x axis. The movement is considered as slow enough so that the velocity is not an influencing factor. A current position of the centre of gravity of a symmetric (along the x axis) obstacle located in front of the sensor, x_o, can be estimated with the formula:

$$x_o = \sum_{i=1}^{n_{PD}} (v_i \cdot x_i) / \sum_{i=1}^{n_{PD}} v_i \,, \tag{4}$$

where v_i is a light intensity value sampled by an i-th photodiode and x_i is the PD's position in the Cartesian coordinate system. The function of the real position of an obstacle along the x axis vs x_o is of interest. Different obstacles and distances, h, should be examined.

The motion detection can be also considered in the time domain. The sampling frequency, f_s, of the sensor defines the upper limit of velocity of the fastest noticeable swipe, V_{not}. It is termed a temporal sensitivity. A sparse linear sensor has to perform at least double sampling during a hand swipe to estimate the velocity of the movement. In the most favourable boundary case, the sensor operating at f_s, performs the sampling at the moment when a hand moving with V_{not} appears above the first and the last photodiodes in the following sampling cycles. The double of f_s ensures the double sampling also in the least favourable case. Therefore, the minimal f_s of the sensor may be expressed as follows:

$$f_s = 2V_{not} / \left((n_{PD} - 1) \cdot d_{PD} \right). \tag{5}$$

As f_s affects power consumption levels it has to be based upon moves performed by the user.

2.3.5. Power consumption

Such parameters as brightness of the LEDs, n_{LED}, a target f_s of the device and a fill factor, D, determine the power consumption of the illumination system of the sensor. D is a duration of the LEDs' turned-on state within the duration of the sampling period. Its value depends on the settling time of applied photodiode chips and the ADC's sampling period duration.

2.4. Monte Carlo simulations

In this work simulations were used to determine different geometrical configurations, sensor element formations and individual parameter adjustment of a virtual optical gesture sensor instead of building many versions of the physical device. Considering the light-solid interactions, employing the *Monte Carlo method-based simulations* (MCMS) is a commonly applied approach [19]. In our study, a simplified interaction model, described in [20], was used. At the initialization stage each photon is given a weight, W, which decreases according to the length of the ray and reflection events. The unitless weight is an equivalent of the amount of energy of a photon. A fixed number of photons, N = 50 million, take part in each simulation. They are generated by the light sources of the modelled sensor, interact with an obstacle and possibly hit one of the detectors. An obstacle can be described by 4 parameters: x_o, y_o, R, and w. A point (x_o, y_o) indicates the position of the centre of obstacle in the described Cartesian coordinate system. R is a radius of the curved part of a round obstacle (*e.g.* finger), whereas the w parameter describes a width of the plane part of the modelled obstacle.

The model solver was designed in Matlab. However, a large number of sampling events led us to implement it within a multithread C# application, which has accelerated the computation approximately 75 times.

2.5. Laboratory experiments

The laboratory experiments were designed and performed to determine the sensor properties and to verify the light interaction model. For this purpose, the sensor described in Subsection 2.1, configured as d_{PD} = 1 cm, β_{PD} = 60° and d_{LED} = 2 cm, β_{LED} = 120°, has been used. During the experiments, the examined light reflecting obstacle was attached to a trolley, which was

Metrol. Meas. Syst., Vol. 24 (2017), No. 4, pp. 617–630.

moving along a straight track at a velocity of 5 cm/s. An *analogue-to-digital converter* unit (ADC) of the microprocessor sampled the signals from photodiodes into 12-bit, 4-digit numbers at a rate of 40 Hz. The output was read by the PC via a UART interface.

2.6. Correspondence between simulations and measurements

The proposed light-solid interaction model was verified. In the first stage the amplitude vs distance relationship was checked. In the experiment, a flat white cardboard was set to move away from the sensor, so a point P travelled a perpendicular path from h_1 to h_2 (Fig. 5a). The trial was reproduced in the simulation environment. The unit-less values from virtual photodiodes were adjusted to match the measured ones, expressed in volts, by minimizing the residual sum of squares (RSS). The objective parameter was a multiplication factor. The amplitudes were averaged from two middle photodiodes of the sensor ($i = 4$, $i = 5$).

In the next step, the angular sensitivity of the virtual sensor was verified. Two different obstacles were set to move along the sensor, at a given h, so a point P travelled a parallel path from x_L to x_R (Fig. 5a). The passing of an obstacle produced light reflection patterns recorded by each PD. Let S^i and M^i be k-sample long vectors with reflection patterns (windowed from the recorded PD signal) from an i-th photodiode, obtained from simulations and measurements, respectively. It is assumed that the pattern associated with the passing is not wider than k samples. S^i and M^i vectors are normalized over max(S) and max(M), respectively. They are compared using the proposed distance parameter:

$$\zeta^i = \sum_{j=s}^{f} \left| (S_j^i - M_j^i) / \max(M_j^i) \right| \cdot k / (f - s), \tag{6}$$

where: k is a length of the analysis window; s and f are indices, which create an analysis sub-window. The sub-window starts/finishes at an index j where the greater of S^i, M^i vectors' values reaches/falls behind the v_{min} (2% of max(M^i)) (Fig. 5b). The value of v_{min} was chosen experimentally. The application of the sub-window makes the comparison of results of narrow and wide shapes relevant when using (6).

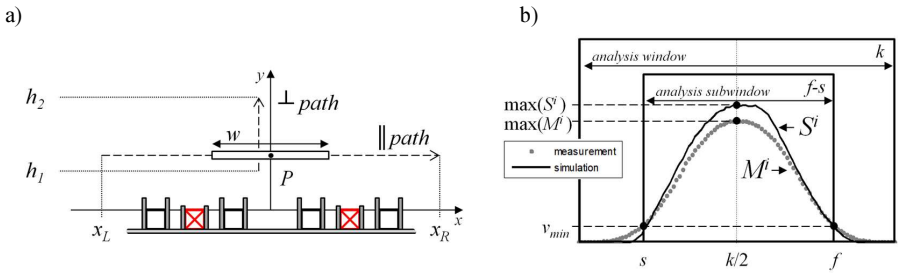

Fig. 5. Parallel and perpendicular paths of an obstacle in relation to the sensor (a). A view of windowed reflection patterns for comparative analysis (idea of the subwindow) (b).

3. Results

3.1. Results of user studies

Distributions of parameters obtained from the control group are presented in Table 2 and in Fig. 6. The results obtained from the control group were applied as the referential data in the research on the related sensor's parameters.

Table 2. Statistical parameters of the control group.

PARAMETER	MEDIAN FEMALES	MEDIAN MALES	MEDIAN TOTAL	STDEV FEMALES	STDEV MALES	STDEV TOTAL
R [cm]	0.7	0.85	0.75	0.05	0.10	0.11
D2 [cm]	2.9	3.6	3.2	0.18	0.30	0.41
L [cm]	3.1	4.0	3.6	0.52	0.65	0.76
AGE [yrs]	23	25.5	24	3.72	7.64	6.11

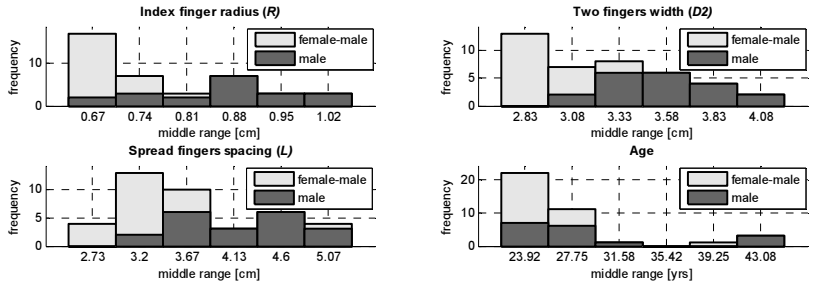

Fig. 6. Characteristics of the control group in a form of histograms.

Perception of speed is a subjective matter. Therefore, the most different values were rejected in order to present compact histograms (Fig. 7) but were included in the statistics (Table 3). Velocities of fast swipes of 2FJ and 2FS were taken together as 2Fx.

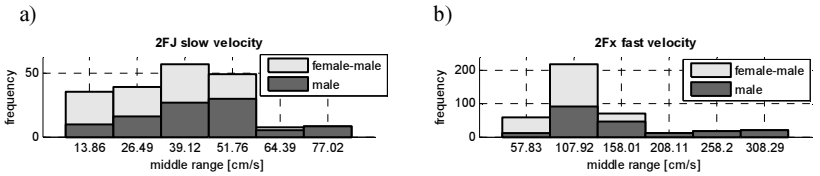

Fig. 7. Distribution of swipe gestures' velocities: 2FJ slow (a); 2FJ and 2FS fast (b).

Table 3. Statistical parameters of gestures performed by the control group.

Gesture	MEDIAN FEMALES	MEDIAN MALES	MEDIAN TOTAL	STDEV FEMALES	STDEV MALES	STDEV TOTAL
2FJ slow [cm/s]	33.90	43.02	37.04	15.85	20.49	19.08
2Fx fast [cm/s]	95.24	125	105.26	37.42	110.53	87.47

3.2. Correspondence between simulations and measurements

The simulations were validated in an amplitude vs distance (h) test using a flat white cardboard of w = 5 cm, to ensure uniform illumination of the middle PDs. An h value varied from 3 to 10 cm. The obtained RSS was equal to 0.48. The formula for the trend function (dashed plot) confirms compatibility of the results with the inverse power law model (Fig. 8).

In the experimental part of angular sensitivity correspondence test, the trolley with an attached obstacle moved 20 times from $x_L = -20$ cm to $x_R = 20$ cm. For each PD a model light intensity pattern, produced by a single passing of an obstacle along the sensor, was arbitrarily chosen. Then, 10 other patterns, most similar to the model pattern upon the correlation coefficient, were selected and averaged, creating M^i vectors. The formula (6) was applied for

Metrol. Meas. Syst., Vol. 24 (2017), No. 4, pp. 617–630.

two white obstacles: a cardboard and a cylinder, as described in Table 4. The table contains the results of how the model corresponds with the reality.

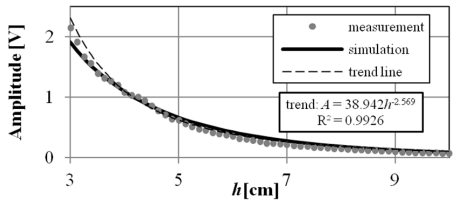

Fig. 8. The amplitude vs distance (h) relationship – real and obtained from the simulated sensor.

Table 4. The distance parameter describing a degree of similarity of simulations and measurements.

photodiode [*i*]	**1**	**2**	**3**	**4**	**5**	**6**	**7**	**8**
ζ^i (cardboard, w = 5 cm, h = 4 cm)	7.09	5.70	3.11	1.79	1.86	4.11	2.01	4.43
ζ^i (cylinder, R = 0.75 cm, h = 2.8 cm)	9.76	9.20	5.68	4.87	5.01	5.28	7.20	7.28

Figure 9 presents the best fitting pair (i = 4) for the cardboard obstacle case (a) and the worst fitting pair (i = 1) for the cylinder obstacle case (b).

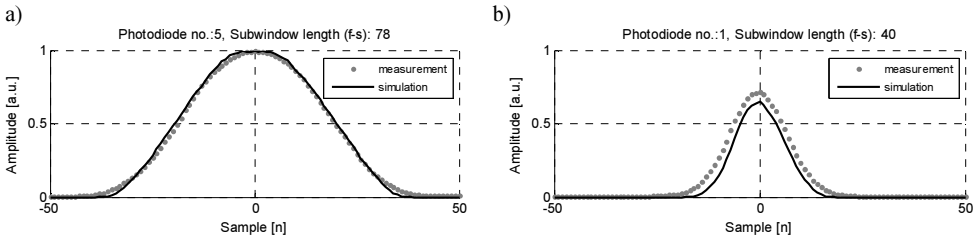

Fig. 9. Comparison of shapes obtained by simulations and measurements in k-sample windows.

3.3. Optical sensor characteristics

The correspondence level of the results obtained from the real world implementation and virtual sensors is high. It enables to accomplish research based on the optical sensor features, which is difficult to perform experimentally, in the elaborated simulation environment.

3.3.1. Illumination pattern

N photons are emitted in simulation by the illumination system of each of the considered formations of the sensor (Fig. 2). Their illumination efficiency can be compared, since the same amount of power is dissipated. The considered flat obstacle was imitating a 2FJ arrangement, w=3.2 cm (median $D2$ from Table 2). In order to narrow the illumination pattern flatness problem, the following parameters were fixed: β_{PD} = 60°, β_{LED} = 120°, n_{PD} = 8 and d_{PD} = 1 cm. Strengths of signals from individual PDs at h = 1 cm produce an illumination pattern (Fig. 10a). The inter-formation highlight efficiency was examined for middle photodiodes of the sensor (Fig. 10b). A single value of $flatness_x$ refers to a given formation of elements and its distance from the sensor, while $flatness_x(h)$ enables to observe flatness of the illumination pattern along both x and y axes (Fig 10 c).

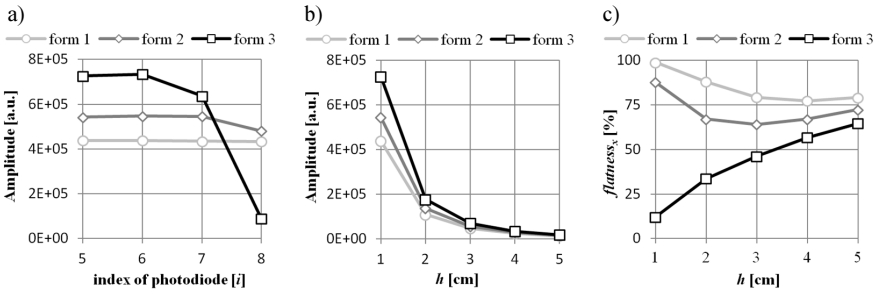

Fig. 10. Strength of the reflected light signals with a 2FJ positioned over a given photodiode at h = 1cm (a). Strength of the reflected light signals from i=5 photodiode as a function of h (b). $Flatness_y$ functions composed of individual $flatness_x$ values (c).

3.3.2. Operating area

A height of the ambiguous zone, h_{op} , has to be kept below h_{min}. With $d_{LED} = 2d_{PD}$, $\beta_{LED} = 120°$ and β_{PD} up to 82° (1), h_{op} is defined by geometry of the detector. The relation d_{PD} vs β_{PD}, based on (1), helps to fulfill the condition $h_{op} \leq h_{min}$ (Fig. 11a, painted area). $l(h)$ depends on a triple: n_{PD}, d_{PD} (cm) and β_{PD}. The value of $l(h)$ was calculated for differently configured sensors, described by 3 triples: (6, 1.4, 80°), (8, 1, 60°) and (10, 0.8, 45°), respectively (Fig. 11b). The values of n_{PD} and d_{PD} from each triple were selected so their products, which mean the separation between the boundary PDs, $l(0)$, are possibly equal. d_{PD} and β_{PD} from the triples respect the relation: $h_{op} \leq h_{min}$. A smaller d_{PD} is not considered due to the size of the photodiode chip.

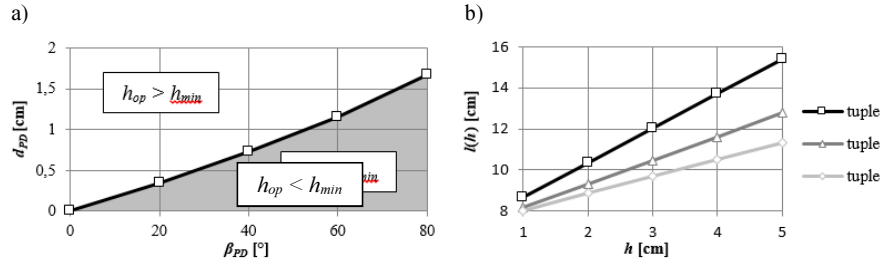

Fig. 11. A function binding values of β_{PD} and d_{PD} to keep h_{op} at a proper level (painted area) (a). The values of $l(h)$ for three different configurations of the sensor, described by three triples (b).

3.3.3. Resolving power

Dependencies of the indentation depth, I_D, were obtained from the simulations. The values of parameters of a 2FS gesture, R and L, corresponded with median values from Table 2. Three virtual sensors described by 3 triples (Subsection 3.2.2), with β_{LED} = 120°, each with a relative placement of PDs and LEDs as in formation 1, were examined. Notice that the 1st and 3rd triple sensors have no LED at the origin in this case (Fig. 1). The $I_D(shift)$ functions at half of the range (h = 3 cm) were calculated upon the obtained simulation results (Fig. 12a). The smallest of local minimums, which are measured between adjacent bulges of the I_D function (marked by a circle in Fig. 12a), is considered as the minimal I_D at a given h, when plotting the min($I_D(shift)$) vs h function (Fig 12b).

Metrol. Meas. Syst., Vol. 24 (2017), No. 4, pp. 617–630.

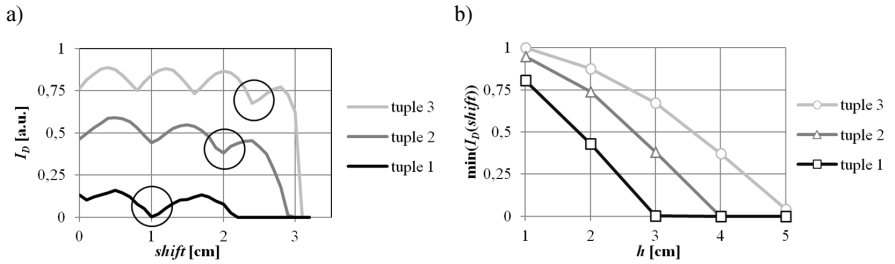

Fig. 12. The $I_D(shift)$ functions calculated for a 2FS located at h = 3 cm for three triples of parameters (a). min($I_D(shift)$) vs h functions for three triples of parameters (b).

3.3.4. Spatial and temporal sensitivity

Three obstacles were considered in the simulation research on spatial sensitivity. The 1FS one was a round obstacle of R = 1.7 cm, whereas 2FJ and 4FJ ones were flat planes of w equal to 3.2 and 6.4 cm (doubled *D2*) respectively. In each trial, the centre of gravity of an obstacle, x_o, was located in a virtual space at (0, h) and the movement along the x axis was simulated, so the *shift* has changed. The virtual sampling was performed after every 0.1 cm of actual *shift*. The calculated *shift* of each obstacle, perceived by the virtual sensor configured as in the 3rd triple (Subsection 3.2.2) of formation 1, at h = 3 cm was obtained upon (4) (Fig. 13a). The standard deviation of the position for different h values was examined for the 2FJ obstacle. It was calculated for *shift* values in ranges of 0–0.5 cm, 0–1 cm up to 0–4 cm (Fig 13b). The 2FJ arrangement was selected as it reflects more light than 1FS and is more precise than 4FJ.

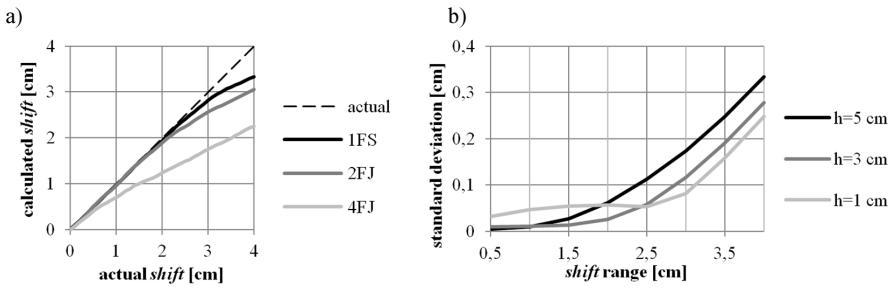

Fig. 13. Calculated *shift* vs actual *shift* for different arrangements at h = 3 cm (a). Standard deviation of position along x axis for 2FJ as a function of h (b).

Table 5 presents the relationship between f_s and V_{not} for the sensor configured according to triple 2 (as the real world implementation). Due to the possibly equal inter-triple products of n_{PD} and d_{PD} the numbers in Table 5 would be at least very similar for other configurations of the sensor. In the summary, the total of 4 cases were examined. Case 1 shows V_{not} for the highest possible f_s value of the device, respecting the required sampling and signal settling times. In cases 2 and 3 V_{not} was selected as the maximal and median velocity of fast swipes, respectively (2Fx fast swipe from the control group). Case 4 shows the noticeable swipe speed for a selected sampling frequency of the gesture sensor, f_s = 40 Hz. Notice how f_s affects the D value and hence the power consumption. The C parameter indicates the percentage of noticeable fast swipes among all of the fast swipes performed by the control group, when a given f_s is applied. Hence, the selected frequency f_s is a compromise between C and D.

Table 5. Relations between a sampling frequency and a detectable swipe velocity.

CASE	GIVEN *Fs* [Hz]	NOTICEABLE SPEED [cm/s]	GIVEN SPEED [cm/s]	REQUIRED *Fs* [Hz]	*C* [%]	*D* [%]
1	2666.67	9333.33	–	–	100	100
2	–	–	666.67	185.19	100	7.14
3	–	–	105.26	29.24	53.4	1.13
4	40	140	–	–	74.9	1.5

3.3.5. Power consumption

Using the real world implementation of the sensor (Fig. 1a, triple 2) the total time required for sampling of 8 channels (LEDs' turned-on period) was measured to be 375µs. Therefore, complying with the selected sampling frequency, f_s = 40 Hz, the resulting D value is 1.5%. In the illumination system of the used sensor 4 LEDs were applied, each consuming a peak current I_p = 30.83 mA. Hence, an illumination system powered by a 123.32 mA peak current consumes the total of 1.85 mA.

4. Discussion and conclusions

Some initial, preliminary results of the examined construction of a sparse sensor were already presented in [7, 21]. However, a more complex analysis of its parameters is presented in the paper.

The simulations reveal significant variation of illumination uniformity at h = 1 cm within formations (Fig. 10a). The inter-formation variability of illumination strength, in an example of one of central photodiodes of the sensor, drops with an increase of h value (Fig. 10b). The analysis indicates formation 1 as the one producing the most flat illumination pattern along both axes (Fig. 10c). It is characterized by very high $flatness_x$, especially in an area close to the sensor (h < 3 cm). Such a sensor also saturates with a reflecting obstacle located closer to the device in comparison with other formations (a wider effective range).

The reported operating distal range of optical sensors often reaches tens of centimetres [4, 11, 14]. However, the proposed sparse sensor is considered to handle unobtrusive gesticulation, performed at a close distance, hence the upper range h_{max} = 5 cm, similar to [17], was assumed to be sufficient. As presented (Fig. 8), the strength of the signal at h_{max} for a 5 cm wide obstacle is still significant, but it saturates at a distance $h > h_{min}$. The strength of the signal depends on the width of the reflecting object, so that the power of the LEDs needs to be adjusted.

The operating area can be controlled by the height of an ambiguous zone ($d_{PD} - \beta_{PD}$ relation) but the parameters of the sensor have to be selected carefully (Fig. 11a).

The resolving power of the sparse sensor enables to differentiate static hand gestures. This is an advantage in comparison with the solutions where the fingers' arrangement can be recognized based only on dynamic gestures [9, 10]. The I_D functions indicate that the sensor configured as the 2nd triple (8, 1, 60°) has a sufficient resolving power at h = 3.5 cm, if a threshold I_{Dt} = 10% is applied. However, the 3rd triple (10, 0.8, 45°) sensor can see FS arrangements almost in the whole considered range ($h \leq h_{max}$). The selectivity of individual PDs (β_{PD}) and the sparse construction of the sensor enable rough differentiation between the widths of light reflecting obstacles; hence also the distinguishing 1FS, 2FJ and 4FJ gestures is plausible.

Common MGSs need a clear swipe in order to detect a hand movement, *e.g.* a 2 cm long one [10]. However, typical interfaces, which are oriented towards the continuous gestures, are able

Metrol. Meas. Syst., Vol. 24 (2017), No. 4, pp. 617–630.

not only to notice a swipe but also to estimate a current location of a hand/finger. The position standard deviation errors in one such interface are equal to 0.03 cm, 0.02 cm, 0.01 cm in the x, y and z axes, respectively [15]. The accuracy of hand localization in the proposed sparse sensor was examined only along the x axis. The results show that for the 2FJ fingers' arrangement the standard deviation of the calculated position is the smallest when the hand operates above the central part of the sensor. In practice, it barely exceeds 0.1 cm for fingers moving within the middle 5 cm of the sensor range ($x_L = -2.5$ cm $x_R = 2.5$ cm), regardless of h (when h value is within the operating distance, $h_{min} \leq h \leq h_{max}$) (Fig. 13b). Therefore, the 2FJ should be considered as the main arrangement for continuous gestures. The obtained resolution, for a basic sensor, which is oriented on both continuous and discrete gestures, is promising but correction methods and localization on the z axis have to be examined.

Considering the detection of swipes of equal velocity, the sensor with a sparse construction can operate roughly at a $(n_{PD}-1)d_{PD}$ times lower f_s in comparison with a single-chip device. Therefore, due to a relatively low sampling rate the current consumption is lower than that reported for many optical sensors in the literature, which can be found in a range of 10-20 mA [4, 9, 10, 11] but 3.78 mA sensors were reported as well [12] (all solutions with 1 LED, enclosed in a single chip). The power consumption was found to be around 8 mW [13, 14], but many sensors consume more than 20 mW [8, 13]. The proposed sparse linear sensor draws 1.85 mA (9.25 mW) for the illumination system. A single PD chip consumes around 20 μA when supplied only during the sampling period. Therefore, the total consumption related with the optoelectronic elements is 2.02 mA (10.1 mW) and 2.16 mA (10.19 mW) for systems with 8 PDs + 4 LEDs (a real world sensor) and 10 PDs + 6 LEDs (the best configuration of a virtual sensor), respectively. The total consumption can be further reduced by application of PDs with shorter settling times.

The proposed construction of sensor delivers two features in terms of gesture recognition: recognizing arrangements of individual fingers formed by a hand [7] and precise localizing a hand in relation to the sensor, regarding two axes. Those features enable to define sets of discrete and continuous gestures [22]. Therefore, basing on the results, the expected interactions between the user and the sensor are as follows: hand swipe events (along 1 axis), movements towards and from the sensor, mouse-like navigation (continuous) and combinations of static hand pose. A low power consumption of the proposed sparse gesture sensor makes it a promising solution for mobile devices. A rich set of gestures handled by the sensor enables to consider it as the main interface to adapted mobile operating systems. The size and shape of the device make it an attractive solution for smart glasses, since it can be easily mounted at a side of the frame as it is usually done [23, 24]. The advantages of the proposed gesture sensor enable to use it within special applications, *e.g.* in the industrial or sterile environment.

Acknowledgements

This work has been partly supported by NCBiR, FWF, SNSF, ANR and FNR in the framework of the ERA-NET CHIST-ERA II, project *eGLASSES – The interactive eyeglasses for mobile, perceptual computing,* and by Statutory Funds of Electronics, Telecommunications and Informatics Faculty, Gdansk University of Technology.

References

[1] Czuszyński, K., Rumiński, J., Kocejko, T., Wtorek, J. (2015). Septic safe interactions with smart glasses in health care. *Proc. of EMBC 2015 Conference*, *IEEE Xplore*, 1604–1607.

[2] Mentis, H.M. (2015). Voice or Gesture in the Operating Room. *Proc. of CHI EA '15 Conference*, *ACM*, 773–780.

[3] Hinckley, K., Pierce, J., Sinclair, M., Horvitz, E. (2000). Sensing Techniques for Mobile Interaction. *Proc. of UIST '00 Symposium ACM*, 91–100.

[4] Metzger, C., Anderson, M., Starner, T. (2004). FreeDigiter : A Contact – free Device for Gesture Control. *Proc. of ISWC '04 Symposium*, *ACM*, 18–21.

[5] Manabe, H. (2013). Multi-touch gesture recognition by single photoreflector. *Proc. of UIST '13 Symposium, ACM*, 15–16.

[6] Gao, Y., Broga, A.M., Krishnaswamy, P. (2015). Contactless gesture recognition with sensor having asymmetric field of view. Patent no. EP 2866124 A1.

[7] Czuszynski, K., Ruminski, J., Wtorek, J., Vogl, A., Haller, M. (2015). Interactions using passive optical proximity detector. *Proc. of HSI 2015 Conference, IEEE Xplore*, 180–186.

[8] Cheng, H., Chen, A.M., Razdan, A., Buller, E. (2011). Contactless Gesture Recognition for Mobile Devices. *MIAA*.

[9] Kim, Y.S., Baek, K. (2013). A motion gesture sensor using photodiodes with limited field-of-view. *Optics Express*, 21(8), 555–560.

[10] Kong, K., Kim, Y.S., Kim, J.E., Kim, S., Baek, K. (2013). Single-Package Motion Gesture Sensor for Portable Applications. *IEEE Transactions on Consumer Electronics*, 59(4), 848–853.

[11] Kim, J.S., Yun, S.J., Seol, D.J., Park, H.J., Kim, Y.S. (2015). An IR Proximity-Based 3D Motion Gesture Sensor for Low-Power Portable Applications. *IEEE Sensors Journal*, 15(12), 7009–7016.

[12] Kim, J.S., Yun, S.J., Kim, Y.S. (2016). Low-power motion gesture sensor with a partially open cavity package. *Optics Express*, 24(10), 10537–10546.

[13] Withana, A., Peiris, R., Samarasekara, N., Nanayakkara, S. (2015). zSense : Enabling Shallow Depth Gesture Recognition for Greater Input Expressivity on Smart Wearables. *Proc. of CHI '15 Conference, ACM*, 3661–3670.

[14] Withana, A., Ransiri, S., Kaluarachchi, T., Singhabahu, C., Shi, Y., Elvitigala, S., Nanayakkara, S. (2016). waveSense : Ultra Low Power Gesture Sensing Based on Selective Volumetric Illumination. *Proc. of UIST '16 Symposium, ACM*, 139–140.

[15] Chuang, C., Chang, T., Jau, P., Chang, F. (2014). Applying the Kalman Filter to the Infrared-Based Touchless Positioning System with Dynamic Adjustment of Measurement Noise Features. *Proc. of IMPACT 2014 Conference, IEEE Xplore*, 84–87.

[16] Tang, S.K., Tseng, W.C., Luo, W.W., Chiu, K.C., Lin, S.T., Liu, Y.P. (2011). Virtual Mouse: A Low Cost Proximity-Based Gestural Pointing Device. *Proc. of HCI 2011Conference, Springer*, 491–499.

[17] Butler, A., Izadi, S. Hodges, S. (2008). SideSight: multi-'touch' interaction around small devices. (2008). *Proc. of UIST '08 Symposium, ACM*, 201–204.

[18] Lewandowski, T., Augustyniak, P. (2010). The System of a Touchfree Personal Computer Navigation by Using the Information on the Human Eye Movements. *Proc. of HSI 2010 Conf., IEEE Xplore*, 674–677.

[19] Zhu, C., Liu, Q. (2013). Review of Monte Carlo modeling of light transport in tissues Review of Monte Carlo modeling of light transport. *Journal of Biomedical Optics*, 18(5), 1–12.

[20] Czuszynski, K., Ruminski, J., Polinski, A. Bujnowski, A. (2016). Estimation of the amplitude of the signal for the active optical gesture sensor with sparse detectors. *Proc. of HSI 2016 Conference, IEEE Xplore*, 483–489.

[21] Bujnowski, A., Czuszynski, K., Ruminski, J., Wtorek, J., McCall, R., Popleteev, A., Louveton, N., Engel, T. (2015). Comparison of active proximity radars for the wearable devices. *Proc. of HSI 2015 Conference, IEEE Xplore*, 158–165.

[22] Czuszynski, K., Ruminski, J., Bujnowski, A., Wtorek, J. (2016). Semi complex navigation with an active optical gesture sensor. *Proc. of UbiComp '16 Conference, ACM*, 269–272.

[23] Amft, O., Wahl, F., Ishimaru, S., Kunze, K. (2015). Making Regular Eyeglasses Smart. *IEEE Pervasive Computing*, 14(3), 32–43.

[24] Serrano, M., Ens, B., Irani, P. (2014). Exploring the Use of Hand-To-Face Input for Interacting with Head-Worn Displays. *Proc. of CHI '14 Conference, ACM*, 3181–3190.